Measuring Hydroelastic Deformation of Very Flexible Floating Structures

Schreier, Sebastian; Jacobi, Gunnar

DOI
10.1007/978-981-16-2256-4_21

Publication date
2022

Document Version
Final published version

Published in
Proceedings of the 2nd World Conference on Floating Solutions, WCFS2020

Measuring Hydroelastic Deformation of Very Flexible Floating Structures

Sebastian Schreier and Gunnar Jacobi

Abstract For Offshore Floating Photovoltaics (OFPV) applications, thin-film PV panels on lightweight floating support structures gain increasing scientific and commercial interest. Over the past years, several different concepts of thin-film OFPV have been proposed, with the common denominator of floating mattress or blanket-like support structures with very little draft in the order of centimeters compared to their width and length in the order of several tens to hundreds of meters. Mostly made from polymer foam materials, these floating support structures are more flexible than the conventional Very Large Floating Structures (VLFS) investigated in 1990s. The flexibility of a floating structure is expressed by the characteristic length derived from the ratio of the structural bending stiffness and the hydrostatic stiffness of the support. For conventional VLFS, this characteristic length is usually longer than the dominant wavelength of the ocean waves, resulting in only moderate structural deflections of the order of 1/10 of the wave height and the total thickness of the structure. The newly proposed structures have characteristic lengths of less than the wavelength of ocean waves. This allows the structures to move with the waves and follow the wave elevation like a floating blanket. Therefore, these structures are classified as Very Flexible Floating Structures (VFFS). Despite the growing interest in VFFS, little is still known about their hydroelastic deformation and their influence on the surrounding wave field. To start the experimental VFFS research at Delft University of Technology, Digital Image Correlation (DIC) measurements were carried out in this study to investigate the vertical deflection of a VFFS at model scale in a small towing. The model's characteristic length was 1/3 of the shortest wavelength and it was tested in long-crested regular longitudinal waves. The wavelength varied between 1/10 and 1/5 of the structure length. The measurements showed that the structure indeed

S. Schreier (✉) · G. Jacobi
Faculty 3mE, Department M&TT, Section SHS, Delft University of Technology, Mekelweg 2, Delft 2628 CD, The Netherlands
e-mail: s.schreier@tudelft.nl

G. Jacobi
e-mail: g.jacobi@tudelft.nl

Ł. Piątek et al. (eds.), *WCFS2020*, Lecture Notes in Civil Engineering 158,
https://doi.org/10.1007/978-981-16-2256-4_21

mostly followed the wave elevation and revealed 3D effects across the structure, which require deeper investigation into wave scattering of VFFS.

Keywords Offshore floating PV · Digital image correlation (DIC) · Hydroelasticity · Wave scattering · Very flexible floating structures (VFFS)

1 Introduction

Over the past decennia, investigation of hydroelastic response of floating structures was mainly motivated by research on sea ice and Very Large Floating Structures (VLFS), see the reviews of Karmakar et al. [1] as well as Squire [2, 3], Chen et al. [4], and Lamas-Pardo et al. [5]. As Squire [6] points out, there are modelling parallels between VLFS and sea ice investigations. On the other hand, Lamas-Pardo et al. [5] observe that none of the designed VLFS have ever been built, with the sole exception of the Mega-Float floating runway [7]. However, these projects did spark the scientific interest and progress in the field of hydroelasticity.

More recently, hydroelasticity receives renewed attention with the rise of (offshore) floating photovoltaics (FPV). Large modular floating structures for rigid PV panels are envisaged in various projects as summarized by Trapani et al. [8]. Flexible structures for FPV based on thin-film PV modules are demonstrated to have technical and economic potential [9, 10]. Jamalludin et al. conclude "that floating solar could be one of the most important ocean structures in the future" [11].

From the aforementioned reviews, it becomes apparent that there is an abundance of theoretical studies on hydroelasticity. However, experimental investigations and data are much less reported. Several experiments related to the Mega-Float VLFS project are reported in the late 1990s. Yago and Endo investigated a 9.75 m long, 1.95 m wide model with a draft of 16.6 mm [12]. Yago et al. conducted 2D experiments with a 50 m long, 5 m wide model with a draft of 10 mm [13]. In both studies, Yago et al. used models made of composite material to tune the model stiffness to match the scaled-down bending stiffness of the full-scale structure, which had horizontal dimensions of 300 m × 60 m and 5000 m 1000 m, respectively. They measured the structure elevation along the centerline of the model with a string-and-pulley system attached to potentiometers at intervals of 0.4 m. Kagemoto et al. employed optical tracking of 4 LEDs along the centerline of their model with length of 2 m and width of 0.5 m [14]. Their model consisted of segmented floating blocks that were attached to a flexible upper deck of 5 mm acrylic glass. Ohta et al. reported on a model test with a 15 m long model related to a full-scale structure of 1200 m in length [15]. Ohmatsu discussed several experiments related to the Mega-Float project [16]. He advised the use of potentiometers for the measurement of the structural deflection and elaborated on the issue of scaling the bending stiffness of the models.

In the field of sea-ice interaction, Squire conducted experiments with an ice-covered wave flume of 2 m × 1 m using an accelerometer to measure the

vertical deflection of the ice cover [17]. Meylan employed 40 pressure transducers along the bottom of a wave flume of 20 m long and 1.83 m wide to investigate the effect of floating flexible sheets on the waves. He used polypropylene (PP) sheets over the full width of the flume with length of 1.22 m and thickness of 3.175 mm as well as 6.35 mm [18]. Sakai and Hanai carried out experiments with polyethylene (PE) sheets of 5 and 20 mm thickness to simulate sea ice in waves in a 2D setup [19]. They measured the vertical displacement of the sheet at several points along the centerline of the model using ultrasonic sensors. Montiel et al. investigated the behavior of compliant floating circular discs in waves [20]. Their models had a radius of 0.72 m and were made from expanded Polyvinylchloride (PVC) material of 3, 5, and 10 mm thickness. They used optical markers distributed over half of the model surface that were individually tracked by a stereoscopic system. Bennetts et al. conducted experiments in a 3D setup using PVC and PP material for their 1 m wide models, which they varied in length between 1 m and 3 m and in thickness from 5 mm to 19 mm and 20 mm, resp. [21]. Sree et al. conducted 2D experiments with viscoelastic sheets motivated by wave-ice interaction of broken ice [22]. They used oil-doped Polydimethylsiloxane (PDMS, target density 940 kg/m^3) and PP as material for their models. The model length was 1 and 2.45 m in an 8 m long, 0.3 m wide wave flume. The tests were carried out in a 2D setup with specimens covering the full width of wave flume. Ultrasonic height probes were used to measure the structural elevation along the centerline of the model. Sree et al. concluded that under the stiffer PP model, wave lengthening occurred compared to the open water wave, while for the longer waves in the experiment, wave shortening was observed under the viscoelastic PDMS models. Both effects could be related to a viscoelastic model presented by Wang and Shen [23]. With common hydroelastic theory, only wave lengthening is expected for conventional VLFS as reported e.g. by Ertekin and Kim [24].

One of the most governing parameters in hydroelastic response of floating structures is the characteristic length λ_c defined by Suzuki and Yoshida [25], which expresses the ratio of structural bending stiffness EI to hydrostatic stiffness of the support k_c according to Eq. (1) [26].

$$\lambda_c = 2\pi \left(\frac{EI}{k_c} \right)^{\frac{1}{4}} \tag{1}$$

where the hydrostatic stiffness of the support is given by Eq. (2) from the density ρ of the water, gravitational acceleration g, and the width B of the beam.

$$k_c = \rho g B \tag{2}$$

Using the material properties reported for the aforementioned experiments at model scale, the characteristic length was calculated. Based on these results, the relative wavelength λ/λ_c was set out against the relative structural length L/λ in Fig. 1 with wavelength λ and structural length L.

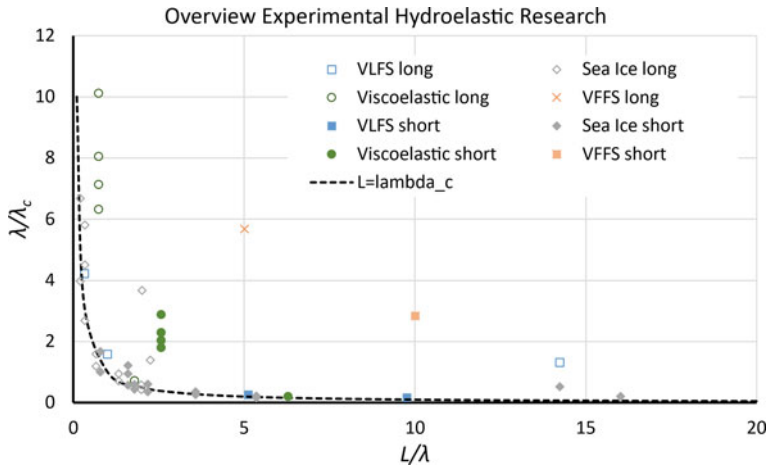

Fig. 1 Overview of experimental hydroelastic research. Open symbols are results with the longest wavelength reported in the references, closed symbols pertain to the shortest wavelength

From the overview in Fig. 1, it becomes apparent that most experiments were conducted at conditions where the characteristic length λ_c was close to the structural length L as indicated by the dashed line representing $L/\lambda_c = 1$. For sea ice, this allocation can be interpreted that ice floes break up at lengths close to their characteristic length. For VLFS, the structural stiffness resulted from the intended application as floating airport and matched well with the characteristics of natural ice. The clustered outliers indicated by the open and closed circles are the viscoelastic models investigated by Sree et al. [22]. The individual open and closed circle located along the dashed line are the reference models of that study made from PP material.

The orange x and square in Fig. 1 mark the model tests of VFFS reported in this study. From this overview it becomes obvious that VFFS have much shorter characteristic length compared to the wavelength than both sea ice and conventional VLFS. Therefore, exploratory model tests with VFFS were carried out to obtain a first impression of their hydroelastic response in waves. For this purpose, we employed a 5 mm thick sheet of neoprene foam in long-crested regular waves and measured the vertical deflection using 3D Digital Image Correlation (DIC).

2 Model Experiments

2.1 Test Setup

The experiments were carried out in the No. 2 towing tank of the Ship Hydromechanics Lab of Delft University of Technology. The tank is 80 m long and

2.75 m wide. Water depth for the experiments was 1.00 m and water temperature was 17 °C. The tank is equipped with a single-paddle wave maker with adjustable hinge point at one end and a wave-damping beach at the other. We used the wave maker in regular flap-type mode with hinge point at the bottom of the tank.

The model structure was a closed-pore neoprene foam rubber sheet of L = 4.95 m long and B = 1.02 m wide with a thickness of h = 5 mm. The density of the neoprene material was 116 kg/m^3. The plate bending stiffness D of the sheet was determined from a static deflection test with a localized load to $D = \frac{Eh^3}{12(1-\nu^2)} = 6.9 \cdot 10^{-3}$Nm. With an assumed Poisson ratio for soft materials of ν = 0.4, the Young's modulus became E = 560 kPa and the characteristic length of this model was λ_c = 0.17 m.

In transverse direction, the model was moored in the center of the tank by four mooring lines connected to the sidewalls of the tank. The front mooring lines towards the wave maker were Dyneema lines with very high stiffness and diameter of 0.2 mm. The aft mooring lines towards the beach were soft mooring lines made from an elastic sewing thread with <1 mm diameter. The aft mooring lines were pre-stretched with an elongation of $\epsilon = \Delta L/L_0 = 15 - 20\%$ resulting in a pretension of 0.1 N and a mooring line stiffness at this elongation of $dF(\epsilon)/d\epsilon = 0.475$N. The mooring lines were attached to the corners of the neoprene sheet by small pad eyes made from a loop of adhesive tape to avoid the load concentration of a hole punched through the model. To further limit the influence of the mooring lines on the structural elevation in waves, the mooring lines were 5 m long and connected to the tank walls to either side of the model at the height of the undisturbed waterline. The longitudinal positions of the mooring connectors on the tank wall are given in Table 1. The setup with stiff front mooring lines and elastic aft lines was chosen to keep the model in the field of view of the cameras without applying excessive pretension on the model.

With the available DIC cameras and the geometric constraints of the laboratory building, it was not possible to bring the whole model structure into the field of view of the cameras. Due to the elaborate camera setup and time-consuming alignment and calibration procedure of the DIC system, we decided to leave the cameras in place and shift the model in the tank to observe the deflections of the full model via repeated test runs. The basic setup is shown in Fig. 2 with the model in its most forward position (position 1), in which the cameras saw the aft section of

Table 1 Longitudinal position (in meters) of wave probes and mooring points with respect to the wave maker flap in its upright position

Position		1	2	3
Wave probe 1	*dwp1* (m)	25.84	25.84	25.84
Wave probe 2	*dwp2* (m)	29.72	29.72	29.72
Wave probe 3	*dwp3* (m)	38.35	38.35	38.35
Front mooring line	*df* (m)	20.85	22.55	24.25
Aft mooring line	*da* (m)	35.94	37.64	39.34
Front model edge	*def* (m)	25.77	27.47	29.17
Aft model edge	*dea* (m)	30.72	32.42	34.12

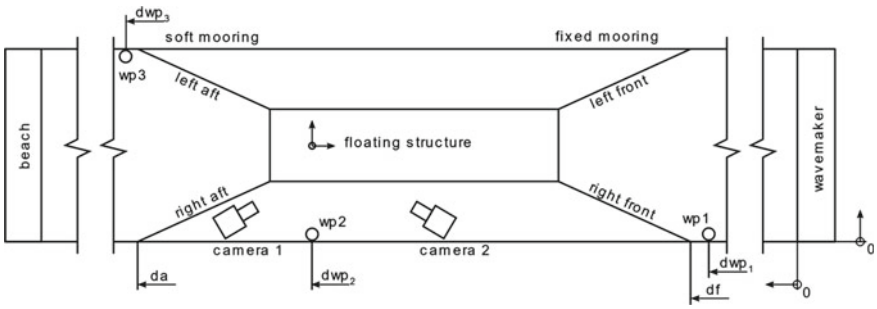

Fig. 2 Plan view of the test setup

the model. In position 2, the mid-section of the model was seen by the cameras, and in position 3, the front section of the model was in the field of view. The model was shifted by relocating the attachment points of the mooring lines on the tank walls in longitudinal direction.

To measure the wave elevation around the model, three resistance-based wave probes WP1-WP3 were placed along the tank wall. WP1 was located between the wavemaker and the model. WP2 was placed next to the model at the field of view of the DIC cameras. WP3 was positioned behind the model towards the beach. The longitudinal positions of wave probes (*dwp1-3*) and mooring points (*df*, *da*) with respect to the wave maker flap in its upright position are summarized in Table 1. A picture of the test setup in the towing tank is shown in Fig. 3.

2.1.1 Wave Probe Calibration

The wave probes were calibrated every morning before the first test run by submerging the probes over a range of 180 mm in steps of 20 mm into the water with 30 s immersion time per step and averaging the results per step over 15 s. The sensitivity was then determined by linear regression of the resulting data points. The correlation coefficient was $R^2 \geq 0.9999$ for all calibrations. The largest offset of a calibration point from the resulting regression line was 0.7% with respect to the calibration range of 180 mm. After calibration, the height of the wave probes was adjusted such that the undisturbed water surface was in the middle of the calibrated range.

2.2 Optical Surface Deformation Measurements

The shape of the floating structure and its deformation under the influence of the incoming waves is determined via Digital Image Correlation (DIC). This is a fully non-intrusive, optical full-field technique, where images of the object under

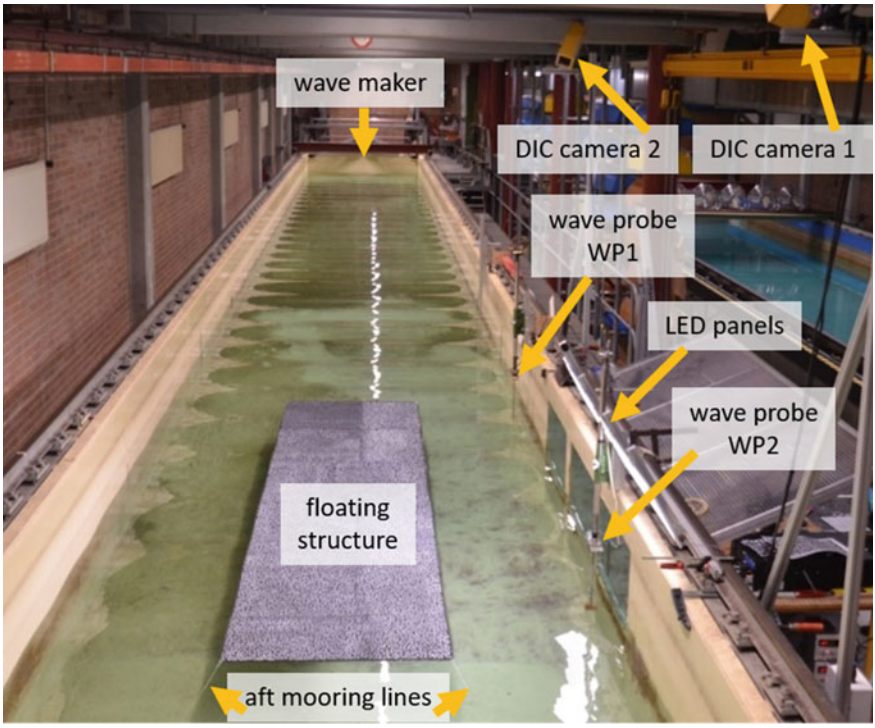

Fig. 3 Test setup in the towing tank

investigation are recorded, and a point-to-point mapping from an undeformed image to the deformed image allows the measurement of the surface displacement [27]. For a successful correlation of successive images, the object surface needs to have a distinct pattern that produces varying intensities of the reflected light. The recorded images are split into subsets to determine the shift of each subset with respect to the reference images. While a single camera setup allows for the measurement of planar deformations, the usage of two or more cameras allows for a reconstruction of the complete three-dimensional deformation vector of the structure by making use of the stereovision principle. The latter was used for the present study, where the initial position of the structure was found from the triangulation of the images of two cameras, and subsequently the deformation was obtained via cross-correlation.

Figure 4 shows the optical setup used for the analysis in this study. The cameras were mounted to the side of the towing tank with a distance of 6 m with respect to each other at a height of 2.5 m above the water surface.

The cameras were LaVision imager MX models with a resolution of 4 megapixels. Equipped with 28 mm lenses and a Scheimpflug adapter, the cameras' field of view covered a model section of 1.8 m. In the current setup, the image

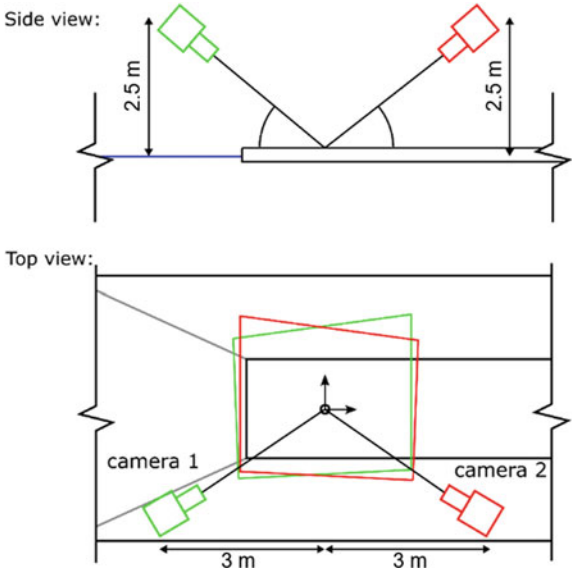

Fig. 4 Optical setup of the DIC system

pixel size was equivalent to 0.7 mm. The general guideline is that the size of speckles should be in the range between 3 and 7 pixels. In this study the size of the speckles applied to the model structure was 9 mm. This yielded an average size of 11–13 pixels per speckle. The model structure with the applied speckle pattern is depicted in Fig. 5. To minimize modification of the mechanical parameters of the neoprene sheet, the speckles were applied with flexible rubber spray paint. For the application of the random pattern, a template of 600 mm × 900 mm was used. To enhance the contrast of the speckle pattern, the measurement area was illuminated with two 45-Watt LED panels.

Fig. 5 Model structure with speckle pattern in the towing tank. Wave propagating from right to left

2.2.1 DIC Calibration

The accuracy of the reconstructed surface elevation depends on the exact determination of the intrinsic and extrinsic parameters of the optical system. These were obtained with a pinhole camera model and a dot-pattern calibration target, which was placed into the field of view prior to the experiments. The size of the target was 1000 mm × 1000 mm with black circular dots on white background in a square grid of 75 mm × 75 mm center to center. The target was carefully aligned with the centerline of the towing tank and the water surface. To enable a comparison of the surface elevation with the data from the wave probes, the center of the calibration target, which defined the model coordinate system, was placed at the longitudinal position of wave probe WP2. Based on the calibration, the images obtained by the DIC cameras were transformed from the image plane back to the real-world coordinate system. In these de-warped images, the model appeared as a rectangle again. Figure 6 shows a de-warped image of the model with its speckle pattern in the tank obtained by camera 1.

2.3 *Test Conditions*

In this study, we investigated the model structure in regular waves with a wavelength λ in the range of $L/\lambda = 5\ldots20$ and wave steepness in the range of $H/\lambda = 0.02\ldots0.05$ based on wave height $H = 2A$, A being the wave amplitude. In this paper we concentrated on the test runs with wavelength $L/\lambda = 5$ and $L/\lambda = 10$. The wave conditions are summarized in Table 2.

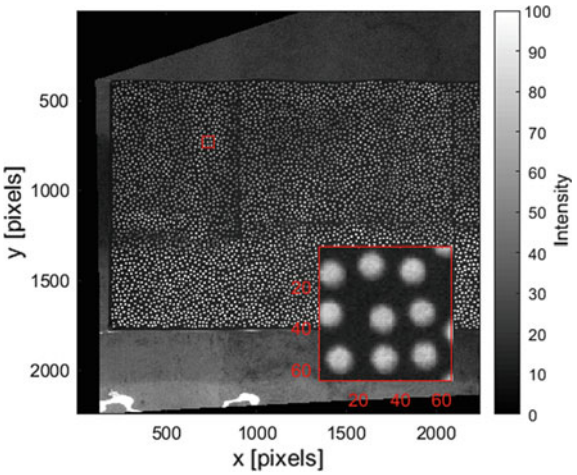

Fig. 6 De-warped image of camera 1 showing the aft section of the model with speckle pattern. Enlarged box illustrates the subset size for DIC measurement and the size of speckles

Table 2 Summary of nominal test conditions

Wave condition	Period	Wavelength	Rel. structure length	Rel. wavelength	Wave amplitude	Wave steepness
	T (s)	λ (m)	L/λ (–)	λ/λ_c (–)	A (mm)	$2A/\lambda$ (–)
W05	0.563	0.495	10.00	2.83	10	0.040
W10	0.796	0.990	5.00	5.67	20	0.040

2.4 Data Acquisition

2.4.1 Wave Probes and Trigger

Each wave probe was connected to its own amplifier, which provided a ± 10 V analogue output signal. For synchronization, a TTL trigger signal with low level of 0 V and high level of 3.5 V was generated, which was linked to the steering signal of the wave maker. This trigger signal was connected to the DIC image acquisition system and was recorded along with the wave probe data.

The wave probe and trigger signals were fed through an analogue low-pass filter with a cut-off frequency of 100 Hz. The filtered signals were then recorded by a data acquisition PC with a National Instruments A/D converter card PCI-6033E at a sampling rate of 1000 Hz and with 16-bit resolution.

2.4.2 DIC Acquisition

The DIC images were recorded by a dedicated image acquisition computer, which controlled the DIC cameras by the DaVis 10 software package from LaVision via the timing unit also provided by LaVision. For sufficient temporal resolution, images were recorded at an acquisition rate of 125 frames per second. This translated to a number of images per wave period of 70.4 for wave condition W05 and 99.5 for wave condition W10. The rising flank of the aforementioned trigger signal started image acquisition.

2.5 Test Procedure

After the model was in position, air bubbles under the model and water accumulations on the model were removed to ensure that all measured deformations were due to the wave and not due to preloading by accidental bubbles under or water on the model. Before each test run with waves and DIC measurements, zero measurements were taken for the wave probes.

The DIC measurement runs were only started when the amplitude of any residual waves in the tank was less than 0.5 mm. Once this condition was met, wave generation and data acquisition for the wave probes and trigger signal were started. The wave generation began with a start-up ramp of 5 s, extended to the next integer multiple of the wave period. After the start-up ramp, monochromatic waves were generated for a duration of 150 wave periods, which was followed by a ramp-down over the same duration as the start-up ramp.

The start trigger for the DIC acquisition was given after the first 50 waves had theoretically passed the wave probe WP2. With the trigger delay, we allowed the wave to develop fully and any start-up effects on the structural deflection to have settled. DIC images were acquired over a duration of 10 s resulting in 1250 images covering 17.8 wave periods for wave condition W05 and 12.6 wave periods for wave condition W10. Figure 7 shows the time series of wave probe WP2 and the trigger starting the DIC acquisition on its rising flank. Furthermore, the timeframe of DIC acquisition is marked with the two red vertical bars.

Data acquisition for wave probes was stopped after 300 s when the last wave had passed the model in all conditions. After each test run, a waiting time was observed until the water in the tank was settled enough to start the next measurement.

Due to the limited camera field of view, the model was shifted in steps to measure the deflections over the entire model. The measurements began with the model in the foremost position 1, in which the DIC cameras were focused on the aft end of the model. After that, we shifted the model in 2 steps of each 1.7 m aft to

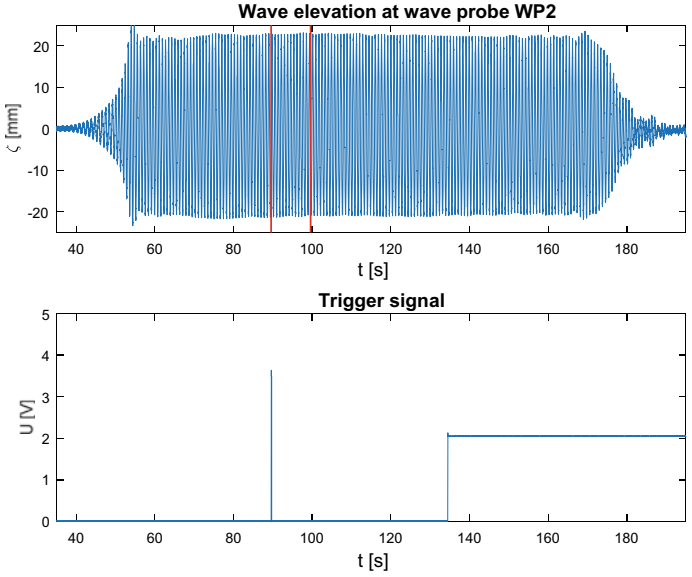

Fig. 7 Time series of wave probe WP2 and DIC trigger showing the DIC acquisition window as the two red vertical bars. Wave condition W10, $L/\lambda = 5$

Table 3 Allocation of test conditions to test runs

Wave condition	Test runs with model in position			
	1	2	3	No model
W05	R48*, R58, R73	R75	R83	R87
W10	R28, R69	R77	R85	R90

*Only DIC data available

positions 2 and 3, where the cameras looked at the mid and front section of the model, respectively.

For reference, one test run per condition was performed without the model in the tank. The allocation of test runs to wave conditions is summarized in Table 3.

2.5.1 Repeatability of Wave Conditions

With the approach to build up the deformation information over the full model from repeated test runs with a shifted model, the test conditions needed to match closely for the individual runs to obtain reasonable results. This repeatability is demonstrated in Figs. 8 and 9 for wave conditions W05 and W10, respectively, by plotting the section of the test runs, which was used for this study, in the same plot. In both figures, the top graph shows the wave elevation ζ at wave probe WP1 in front of the model normalized by the actual wave amplitude per test run, while the bottom graph shows the normalized wave elevation at wave probe WP2 at the longitudinal center of the camera field of view. In all four plots of these figures, the waves show good repeatability. Per plot, the five lines were in almost perfect agreement with the same period and amplitudes, which were within 1 mm of each other.

2.6 Data Processing

For the wave probes, the processing was limited to removing the initial offset in the water level, trimming the signals to the DIC acquisition window, and removing a small time shift between the signals. The resulting signals are shown in Figs. 8 and 9 normalized by the actual wave amplitude per run, which are given in Fig. 11.

The recorded DIC images were processed with the Strain Master package from LaVision. For this processing, the subset size was chosen to 63 pixels with a step size of 21 pixels. With one pixel corresponding to 0.7 mm, this resulted in a final spatial resolution of 15 mm or 33 data points along the shorter wavelength investigated in this paper. Over the model in the camera field of view, a total of 65×120 data points was obtained.

The surface elevation reconstruction was carried out in two steps. First the initial location of the surface was obtained by a triangulation of the reference image taken before the test run. Subsequently, the displacement per subset area was obtained by

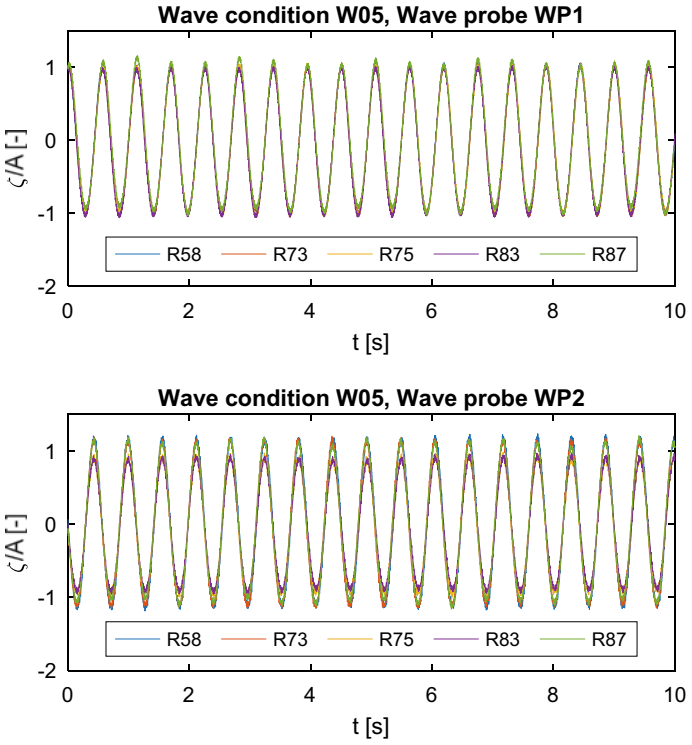

Fig. 8 Repeatability of generated waves. Wave condition W05, $L/\lambda = 10$

cross correlation of the images. Based on this displacement per subset, the elevation of the model surface was reconstructed. Figure 10 shows a 3D representation of the deformed model with the speckle pattern overlaid with the color-coded surface elevation.

For further assessment, the surface elevation fields obtained from Strain Master calculations were exported to Matlab. As a first step, the elevation was plotted as surface plots over the observed area of the model per model position. Figure 11 shows a snapshot per test run with wave condition W05 in the left column and wave condition W10 in the right one. From top to bottom, the plots show the aft, mid, and front section of the model, respectively. In all graphs, the structure elevation was normalized by the actual wave amplitude A of the incoming wave.

Along the edges of the model, the displacement calculations were somewhat spotty, depending on the distance of the first speckles from the edge. These frayed edges can be seen in Fig. 10. For further presentation of the model surface elevation, the longitudinal edges were trimmed down to the area with continuous data available. At the front and aft edge, the blank spots remained in the data sets and can be seen e.g. on the right edge in Fig. 11 for runs R83 and R85.

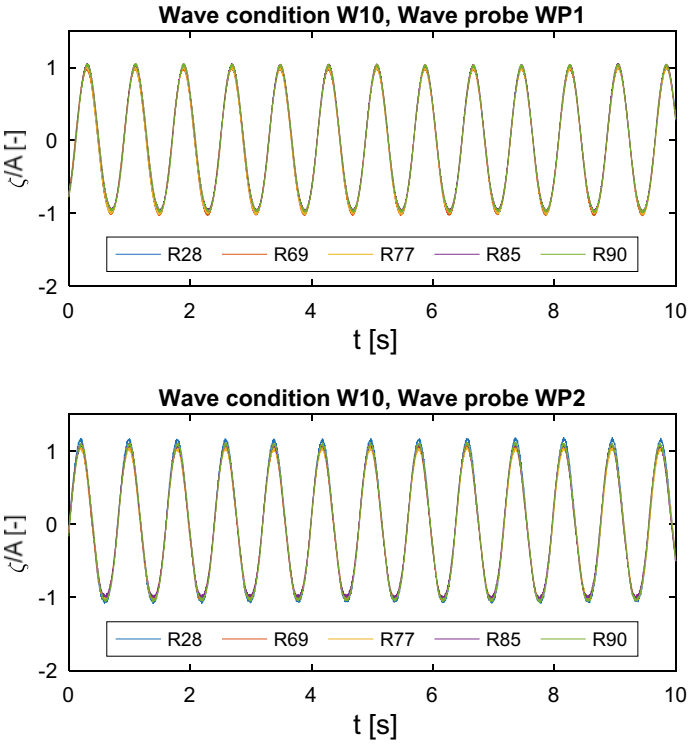

Fig. 9 Repeatability of generated waves. Wave condition W10, $L/\lambda = 5$

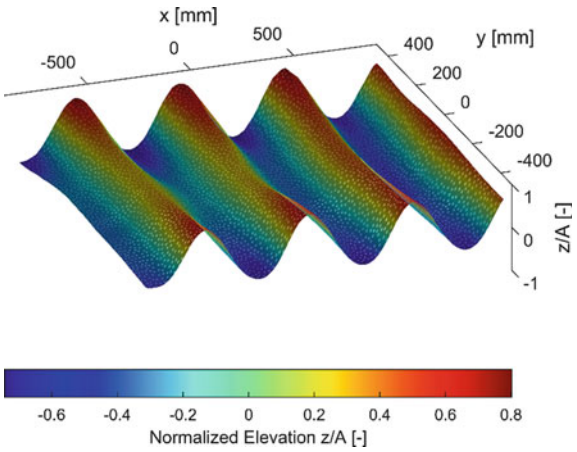

Fig. 10 Superposition of DIC results for model surface elevation and deformed model in waves. Wave propagation from right to left. Wave condition W05, $L/\lambda = 10$

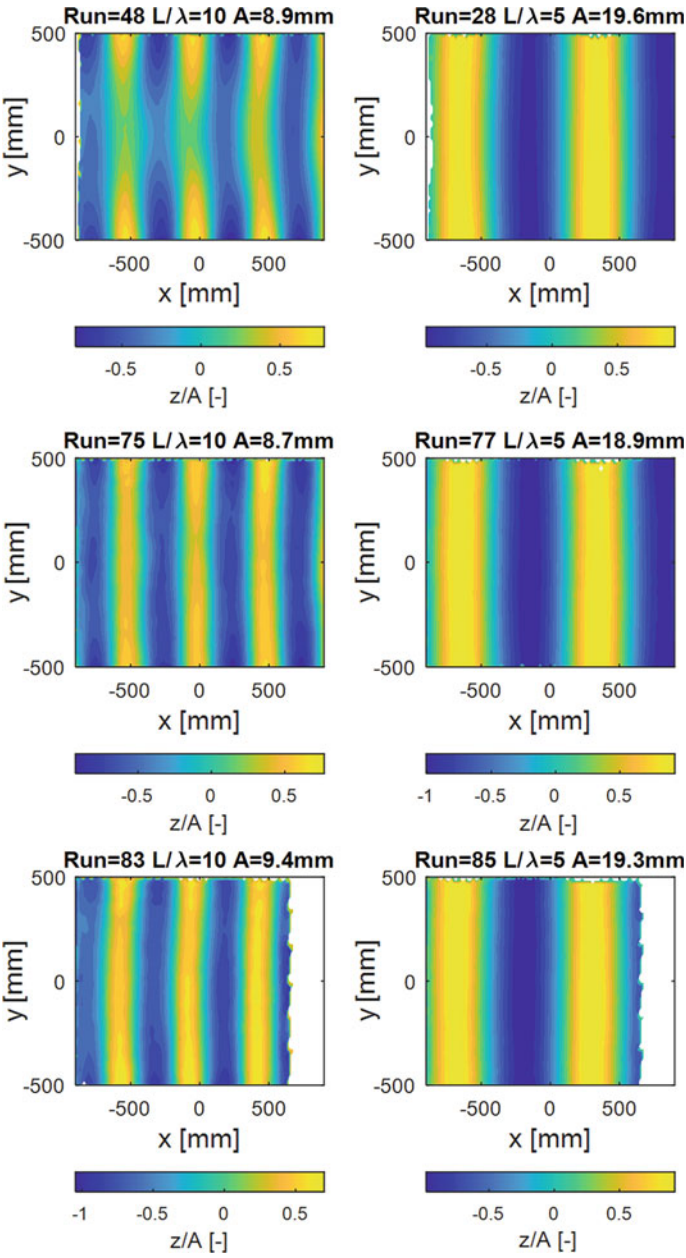

Fig. 11 DIC results of model surface elevation. From top to bottom, snapshots of individual DIC runs looking at the aft, mid, and front section of the model. Left column: wave condition W05, $L/\lambda = 10$, right column: wave condition W10, $L/\lambda = 5$. Wave propagation from right to left

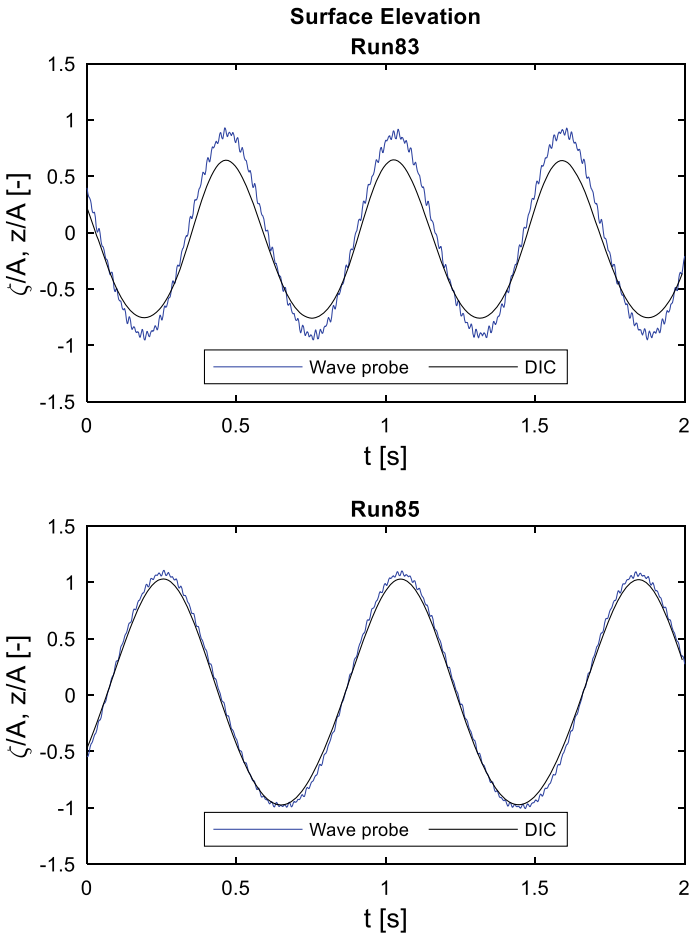

Fig. 12 Comparison of structure elevation and wave elevation at longitudinal position of wave probe 2. Top: run R83, W05, L/λ = 10; bottom: run R85, W10, L/λ = 5

To compare the structure elevation with the wave elevation around the model, a time trace of the structure elevation at the centerline of the model at the longitudinal position of wave probe WP2 was generated from the DIC results. This time trace was then plotted together with the time trace of the wave elevation obtained from wave probe WP2. The resulting plot is shown in Fig. 12.

For the investigation of the surface elevation over the entire length of the model, the three elevation fields per model of Fig. 11 were stitched together in Matlab to one elevation field per model. Given that the camera field of view was fixed with respect to the tank as well as the wave probe WP2 and the model was moved aft through the field of view of the cameras, there was a phase shift between the model and the repeated wave trains. During the DIC acquisition window, the waves were in a

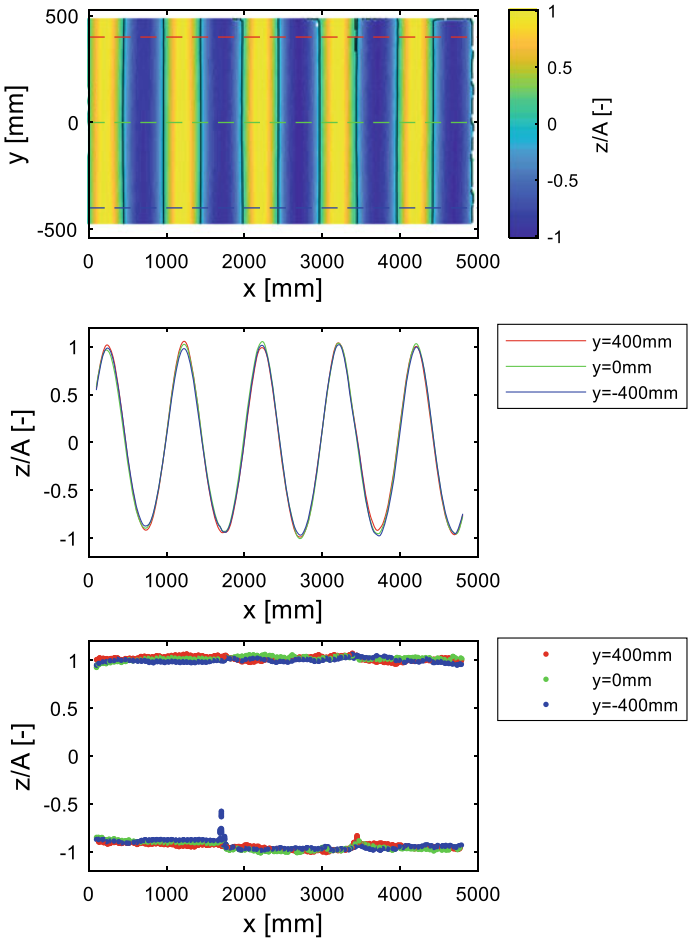

Fig. 13 DIC results for wave condition W10, $L/\lambda = 5$. From top to bottom: surface elevation, elevation profiles, and envelope curves of elevation profiles. Wave propagation from right to left. Surface elevation normalized by actual wave amplitude A

steady-state condition as can be seen from the constant amplitudes in Figs. 8 and 9 as well as Fig. 7. Therefore, the displacement fields were only phase-shifted to match the phase of the neighboring displacement field and not exactly the particular wave of the repeated wave train. To highlight the wave shape of the structure elevation, the $z/A = 0$ contour was marked in the model surface elevation plots. Snapshots of the resulting images are shown in the top graphs of Figs. 13 and 14.

To look into possible variations over the width of the model, three elevation profiles along a longitudinal line down the length of the model were generated. The profiles were taken at the centerline as well as 400 mm to either side of it. The location of the elevation profiles in the model are marked with the dashed lines in

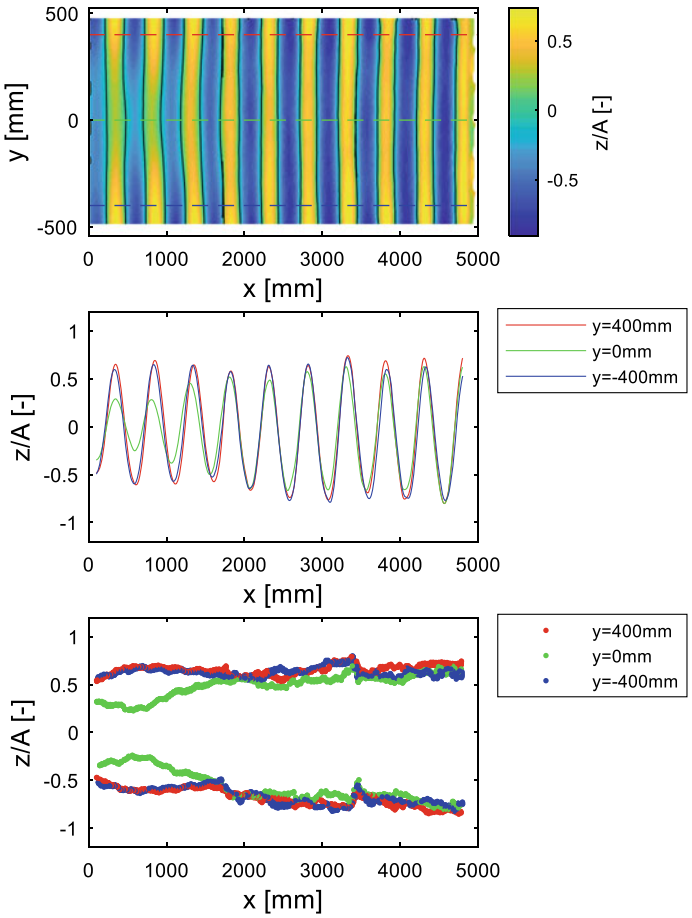

Fig. 14 DIC results for wave condition W05, $L/\lambda = 10$. From top to bottom: surface elevation, elevation profiles, and envelope curves of elevation profiles. Wave propagation from right to left. Surface elevation normalized by actual wave amplitude A

the surface elevation graphs. Snapshots of the surface elevation profiles are shown in the middle graphs of Figs. 13 and 14.

The elevation profiles were also used to assess the repeatability of the structure elevation in repeated wave conditions. For this purpose, the elevation profiles of the aft section of the model were plotted together in one plot for two repeated test runs of both wave condition W05 and W10 in Fig. 15.

For the evaluation of the spatiotemporal evolution of the surface elevation over several wave periods and the entire length of the model, the envelope curves of the elevation peaks and troughs along the profile lines were drawn. These envelope curves were generated by applying a Matlab peak finding algorithm to the elevation

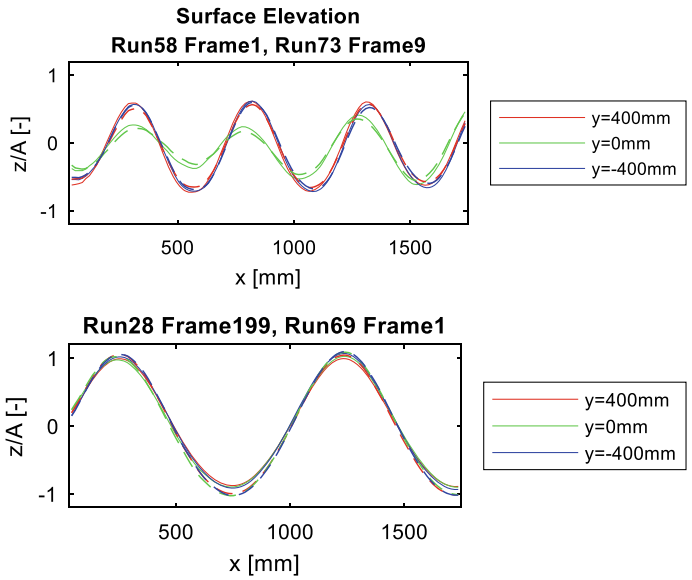

Fig. 15 Repeatability of structure elevation profiles of the aft section of the model for each two test runs with repeated wave condition. Top: runs R58 (continuous lines) and R73 (dashed lines), W05, $L/\lambda = 10$; bottom: runs R28 (continuous lines) and R69 (dashed lines), W10, $L/\lambda = 5$. Wave propagation from right to left

profiles per time step. The accumulated data of all time steps is shown in the bottom graph of Figs. 13 and 14.

3 Results

The results are presented in four steps. First, the elevation of the structure and the waves is evaluated in one location for both wave conditions W10 and W05. Then the surface elevation over the entire model is assessed in consecutive order for wave condition W10 and W05. Eventually, the repeatability of the structural response in addressed.

As can be seen from the right column of Fig. 11, the surface elevation of the model from the DIC measurements for wave condition W10 showed an amplitude closely matching the wave amplitude. This is also visible in the bottom graph of Fig. 12 showing the results of test run R85 with wave condition W10, while the top graph was taken from test run R83 with wave condition W05. For both wave conditions, both wave elevation (blue line) and surface elevation (black line) of the model showed a harmonic oscillation with the same frequency. The elevation amplitude in both cases was smaller than the measured wave amplitude. This effect was more pronounced with the smaller and shorter waves in the top graph of

Fig. 12, and was barely visible for the longer waves of run R85 in the bottom graph of this figure. This was a clear indication of a hydroelastic interaction between the model structure and the shorter wave. However, for this particular model, the details of this interaction are not known yet and require further investigation.

3.1 Wave Condition W10

The overview of the results from the DIC measurements with wave condition W10 with $L/\lambda = 5$, $\lambda/\lambda_c = 5.67$ and nominal wave amplitude $A = 20$ mm is given in Fig. 13. In the top graph of this figure, the surface elevation of the model is shown over the entire measured surface of the model with yellow and blue colors indicating wave crests and troughs, respectively. In all three plots of this figure, the origin of the x-axis coincides with the aft edge of the model. The waves propagated into the negative x-direction from right to left. From this graph, it is clearly visible that there were five wavelengths covering the length of the model. The $z/A = 0$ elevation contours are straight vertical lines in this graph, indicating that the waves propagated under the model as the 2D long-crested waves as they arrived at the model.

This assessment is supported by the elevation profiles over the length of the model depicted in the middle graph, with their location indicated in dashed lines in the top graph. The color of the profile line corresponds to the color of the dashed line, with a green line indicating the profile along the centerline and red and blue lines representing the profiles at $y = 400$ mm and $y = -400$ mm, respectively. In this wave condition, all three elevation profiles match perfectly with normalized amplitudes of 1.0 and exactly the same wavelength. There are only minor deviations at the crests and troughs. These are especially visible at the crest around $x = 1250$ mm and the trough around $x = 3700$ mm. Looking at the five troughs in this graph, a slight upward trend can be noted following the waves from right to left. This indicates that the wave trough got slightly shallower over the length of the model.

The bottom graph of Fig. 13 confirms that there was little change of the waves over the length of the model. The envelope curves of crests and troughs in the model surface elevation are depicted with the same colors as their corresponding elevation profiles. There are hardly any differences between the three lines over the width of the model. The few outliers in the curve for $y = -400$ mm at $x = 1700$ mm are an artifact that can be attributed to the stitching of the results of different test runs. At closer inspection, the rising trend of the troughs in wave propagation direction is confirmed, though the difference from first to last wave trough is only 5–10% of the actual wave amplitude. Close to the aft edge of the model, both elevation crests and troughs show a reduced magnitude. However, also this is only a minor effect.

Based on these results, the structure appeared to have little impact on the waves passing underneath it for the wave condition W10 with the longer waves considered in this study at relative structural length of $L/\lambda = 5$ and relative wavelength of $\lambda/\lambda_c = 5.67$.

3.2 Wave Condition W05

In Fig. 14, the overview of the DIC measurement results is shown for the wave condition W05 with $L/\lambda = 10$, $\lambda/\lambda_c = 2.83$ and nominal wave amplitude $A = 10$ mm. The figure follows the same structure and color-coding as Fig. 13.

In the top graph of Fig. 14, the 10 wavelengths over the length of the model are clearly visible. Following the wave propagation along the model from right to left, increasing 3D effects on the wave shape become apparent. While the crests were highest and the troughs were deepest at the sides of the model, the elevation amplitude reduced towards the centerline. Furthermore, the $z/A = 0$ elevation contours were not straight vertical line anymore but were bent towards the center of the model. For the first 4 wavelengths, i.e. for $x > 3000$ mm, the wave front showed a convex shape with the contour line at the center being more advanced than towards the sides of the model. Then there was a zone of 2000 mm $< x <$ 3000 mm, where the wave contours were almost straight lines. Towards the aft end of the model, the 3D effects became more pronounced with more clearly visible convex shape of the wave contours at 600 mm $< x <$ 2000 mm. The very last wave in the model even shows a concave shape with the crest at the center lagging behind the crest at the sides. These increased 3D effects went along with a reduced wave amplitude, which was more pronounced around the centerline compared to the sides of the model.

The elevation profiles and the envelope curves confirm the presences of 3D effects in the surface elevation. Over roughly the front half of the model, there was only a small phase shift between the elevation profile at the centerline and the two profiles at the sides. The elevation amplitude was only slightly smaller at the centerline than at the sides. In the aft part, for 600 mm $< x <$ 1800 mm, the green curve of the surface elevation at the centerline was clearly shifted towards the left in this graph, thus indicating an increased wavelength at the center of the model compared to the sides. At the same time, the elevation amplitude at the centerline is only half that at the sides of the model. Over the whole length of the model, there is good lateral symmetry in the surface elevation of the model, with the elevation profiles at $y = \pm 400$ mm matching well with each other.

The envelope curves underline the good lateral symmetry of the model surface elevation and only show small differences between the sides and the center over the front 2/3 of the model. Over this part of the model, the elevation crests and troughs reduce almost linearly with the distance of the waves travelled under the model. Over the aft 1/3 of the model length, the sides and center showed opposing trends. While the crest height and trough depth continued to reduce at a higher rate in the

center for 500 mm < x < 1500 mm, the crest height and trough depth increased at the sides. Thus, the differences between center and sides increased. Over the aft 500 mm, i.e. the last wavelength under the model, both trends reversed again and the difference in crest and trough height reduced towards the aft edge of the model. Around x = 500 mm, the difference was largest, such that the elevation amplitude at the center was only about half that at the sides. This confirmed that the profile of the snapshot in the upper two graphs were representative of the general evolution of the model surface elevation.

For this wave condition W05 with relative structural length L/λ = 10 and relative wavelength of λ/λ_c = 2.83, a clear impact of the structure on the waves underneath it is visible from the DIC measurements.

3.3 Repeatability of Structure Elevation

The repeatability of the wave conditions was established in Figs. 8 and 9. In Fig. 15, the surface elevation profiles were plotted for two repeated test runs with wave condition W05 (top) and wave condition W10 (bottom) over the aft section of the model. As in Fig. 14, also in the top graph of Fig. 15, there was a clear difference for condition W05 between the profile along the centerline shown with the green line and the elevation profiles at the side of the model, indicated by the red and blue lines. However, at the same position in the model, there was only a small difference between the results of test run R58, shown by the continuous lines, and test run R73, represented by the dashed lines. In the bottom graph of Fig. 15, the results for wave condition W10 from test run R28, shown in continuous lines, and test run R69, plotted with dashed lines, agree even better. Furthermore, as expected from Fig. 13, there was hardly any difference in the results for wave condition W10 over the width of the model. This indicates that repeatable test conditions indeed led to repeatable test results.

4 Discussion

Compared to the results with wave condition W10, the shorter waves of wave condition W05 clearly experience a stronger hydroelastic interaction with the structure. The increased wavelength and reduced elevation amplitude at the center towards the aft edge of the model suggest that wave spreading occurred for the shorter waves.

While the wave steepness was the same for both conditions, the curvature of the waves and thus also of the neoprene sheet was larger for the shorter waves. Furthermore, there were twice as many wavelengths over the length of the model for the shorter waves. Therefore, there was more time for each wave to interact with the structure. Adding to this effect is the shorter relative wavelength compared to

the characteristic length, which means that the shorter waves led to relatively stronger bending reaction of the structure.

The build-up of 3D effects was also shown by Ertekin and Kim [24] in their study. However, at the aft edge, they report a larger elevation amplitude in the center than at the sides, which is the opposite of what we found in our experiment. In this comparison it needs to be noted that the structure investigated in by Ertekin and Kim had a characteristic length of $\lambda_c = 400$ m for a structure length and width of $L = 5000$ m and $B = 1000$ m, respectively. Therefore, the ratio of structure width to characteristic length was $B/\lambda_c = 2.5$ for their model as compared to $B/\lambda_c = 6$ for the model employed in this paper. Thus, the model presented here is more flexible in transverse direction.

Since the focus of this paper is on the application of the DIC technique for the measurement of surface elevation of flexible floating structures, the results are not discussed in more detail against available theoretical results.

5 Conclusions

In this study, we applied DIC technique to measure the deformation of a floating flexible neoprene foam rubber sheet of 5 mm thickness and 4.95 m length in regular waves in a 3D setup. We demonstrated that wave conditions and results were repeatable. The measurement results showed that the model could follow long-crested waves with an amplitude of 20 mm and wavelength of 0.99 m ($L/\lambda = 5$) without noticeable effects on the waves.

For shorter waves with the same wave steepness, there was considerable hydroelastic interaction between the wave and the model, and 3D effects were detected in the surface elevation of the model. These 3D effects partially matched the effects reported in literature. However, there is disagreement with the literature results regarding the distribution of the elevation amplitude over the width of the model close to the aft edge. This and other effects of wave scattering require further investigation in future studies.

In the presented study, the DIC technique was found to be a promising tool to measure the surface elevation of large flexible floating structures in a towing tank. However, especially with deformations much larger than the thickness of the model, careful consideration needs to be given to the accuracy of this measurement technique. The development and application of appropriate procedures to ensure accurate measurement of large out-of-plane deformations will be the next steps to make DIC a versatile measurement technique for very flexible floating structures.

Acknowledgements The authors express their gratitude to LaVision GmbH for providing the DIC license to the DaVis software.

References

1. Karmakar D, Bhattacharjee J, Sahoo T (2011) Contemporary approaches in the hydroelastic analysis of floating and submerged structures. Mar Technol Eng 1:461–478
2. Squire VA (2007) Of ocean waves and sea-ice revisited. Cold Reg Sci Technol 49:110–133
3. Squire VA (2011) Past, present and impendent hydroelastic challenges in the polar and subpolar seas. Philos Trans R Soc A Math Phys Eng Sci 369:2813–2831
4. Chen X, Wu Y, Cui W, Jensen JJ (2006) Review of hydroelasticity theories for global response of marine structures. Ocean Eng 33:439–457
5. Lamas-Pardo M, Iglesias G, Carral L (2015) A review of very large floating structures (VLFS) for coastal and offshore uses. Ocean Eng 109:677–690
6. Squire VA (2008) Synergies between VLFS hydroelasticity and sea-ice research. Proc Int Offshore Polar Eng Conf 8:1–13
7. Suzuki H (2005) Overview of megafloat: concept, design criteria, analysis, and design. Mar Struct 18:111–132
8. Trapani K, Redón Santafé M (2015) A review of floating photovoltaic installations: 2007–2013. Prog Photovoltaics Res Appl 23:524–532
9. Trapani K, Millar DL, Smith HCM (2013) Novel offshore application of photovoltaics in comparison to conventional marine renewable energy technologies. Renew Energy 50:879–888
10. Trapani K, Millar DL (2014) The thin film flexible floating PV (T3F-PV) array: the concept and development of the prototype. Renew Energy 71:43–50
11. Jamalludin MAS et al (2019) Potential of floating solar technology in Malaysia. Int J Power Electron Drive Syst 10:1638–1644
12. Yago K, Endo H (1996) On the hydoroelastic response of box-shaped floating structure with shallow draft. J Soc Nav Archit Japan 1996:341–352
13. Yago K, Ohmatsu S, Endo H (1997) On the Hydroelastic response of box-shaped floating structure with shallow draft. J Soc Nav Archit Japan 1997:307–317
14. Kagemoto H, Fujino M, Murai M (1998) Theoretical and experimental predictions of the hydroelastic response of a very large floating structure in waves. Appl Ocean Res 20:135–144
15. Ohta M, Ikegami K, Yamaguchi Y (1998) Experimental study on elastic behavior of a huge floating structure in waves (in Japanese). Trans West-Japan Soc Nav Archit 99–108
16. Ohmatsu S (2008) Model experiments for VLFS. In: Wang CM, Watanabe E, Utsunomiya T (eds) Very large floating structures, pp 141–164. Taylor & Francis
17. Squire VA (1984) A theoretical, laboratory, and field study of ice-coupled waves. J Geophys Res 89:8069–8079
18. Meylan MH (1993) The behaviour of sea ice in ocean waves. University of Otago
19. Sakai S, Hanai K (2002) Empirical formula of dispersion relation of waves in sea ice. Ice Environ Proc 16th IAHR Int Symp Ice 327–335
20. Montiel F et al (2013) Hydroelastic response of floating elastic discs to regular waves. Part 1. wave basin experiments. J Fluid Mech 723:604–628
21. Bennetts LG et al (2015) An idealised experimental model of ocean surface wave transmission by an ice floe. Ocean Model 96:85–92
22. Sree DKK, Law AWK, Shen HH (2017) An experimental study on the interactions between surface waves and floating viscoelastic covers. Wave Motion 70:195–208
23. Wang R, Shen HH (2010) Gravity waves propagating into an ice-covered ocean: a viscoelastic model. J Geophys Res 115:C06024
24. Ertekin RC, Kim JW (1999) Hydroelastic response of a floating mat-type structure in oblique, shallow-water waves. J Sh Res 43:241–254
25. Suzuki H, Yoshida K (1996) Design flow and strategy for safety of very large floating structure. Proc Int Workshop Very Large Floating Struct VLFS 96:21–27

26. Suzuki H et al (2006) Very large floating structures. In: Proc ISSC2006: volume 2: structures, safety and reliability; petroleum technology symposium vol 2, pp 391–442. ASMEDC
27. Sutton MA, McNeill SR, Helm JD, Chao YJ (2000) Advances in two-dimensional and three-dimensional computer vision. In: Rastogi PK (ed) Photomechanics, topics in applied physics, pp 323–372. Springer